Machine-learning-assisted fabrication: Bayesian optimization of laser-induced graphene patterning using in-situ Raman analysis

Hud Wahab [a, b], Vivek Jain [a, b], Alexander Scott Tyrrell [a, b], Michael Alan Seas [a], Lars Kotthoff [b, c], Patrick Alfred Johnson [a, b, *]

[a] Department of Chemical Engineering, University of Wyoming, Laramie, WY 82071 USA
[b] Artificially Intelligent Manufacturing Center, University of Wyoming, Laramie, WY 82071, USA
[c] Department of Computer Science, University of Wyoming, Laramie, WY 82071, USA

ARTICLE INFO

ABSTRACT

The control of the physical, chemical, and electronic properties of laser-induced graphene (LIG) is crucial in the fabrication of flexible electronic devices. However, the optimization of LIG production is time-consuming and costly. Here, we demonstrate state-of-the-art automated parameter tuning techniques using Bayesian optimization to advance rapid single-step laser patterning and structuring capabilities with a view to fabricate graphene-based electronic devices. In particular, a large search space of parameters for LIG explored efficiently. As a result, high-quality LIG patterns exhibiting high Raman G/D ratios at least a factor of four larger than those found in the literature were achieved within 50 optimization iterations in which the laser power, irradiation time, pressure and type of gas were optimized. Human-interpretable conclusions may be derived from our machine learning model to aid our understanding of the underlying mechanism for substrate-dependent LIG growth, e.g. high-quality graphene patterns are obtained at low and high gas pressures for quartz and polyimide, respectively. Our Bayesian optimization search method allows for an efficient experimental design that is independent of the experience and skills of individual researchers, while reducing experimental time and cost and accelerating materials research.

© 2020 Elsevier Ltd. All rights reserved.

1. Introduction

Laser materials processing techniques are powerful tools in materials manufacturing [1–3]. Such approaches have also been applied to form graphene [4,5], a two-dimensional material with extraordinary physical and chemical properties [6]. Ground-breaking work focused on direct laser writing of graphene oxide (GO), a graphene derivative that can be mass-produced via wet chemical pathways [4,7,8]. Laser reduction of GO removes insulating oxygen functional groups with precision, which enables micro-patterning and structuring capabilities that are essential for the production of graphene-based electronics [9]. Recently, laser-induced graphene (LIG) patterned on polyimides (PI) substrates has shown potential in fabricating flexible electronic devices [10]. Following the discovery of LIG, precise control over its physical, chemical and electronic properties would allow to broaden the scope of its applications to new areas such as micro-supercapacitors [11,12] and fuel cell technology [13]. Therefore, there is considerable interest in advancing strategies for property engineering of LIG; in particular, optimizing the lasing parameters and the local environment for different substrates allows to control its composition and morphology.

An optimization study is typically concerned with optimizing an objective function that yields a response depending on the values of a given set of parameters. A straightforward strategy for such optimizations is grid search, whereby the parameter space is subdivided into a grid and configurations on this grid are sampled for evaluation. Although grid search is successful for experimental design [3,14,15], it is often an inefficient strategy with real-valued and dependent parameters in larger dimensions. For example, the Taguchi approach constructs the objective landscape with orthogonal arrays, in which parameter inputs are divided *a priori* into a grid of possible values [15], while the Fisher method assumes that parameters take discrete values [14], such that optimal points that

* Corresponding author. Department of Chemical Engineering, University of Wyoming, Laramie, WY 82071, USA.
E-mail address: pjohns27@uwyo.edu (P.A. Johnson).

lie between grid points are not taken into account and thus crucial features of the objective landscape can be overlooked. Consequently, such traditional strategies require a vast number of experimentations or computations to sample on a grid that is sufficiently fine, and thus are not suitable for optimization studies in which evaluations of the objective function are expensive.

The laser reduction parameters are typically optimized using manual trial and error as an exhaustive grid search is infeasible, and the efficiency of the optimization and end result vary depending on the expertise of the individual performing the optimization. In contrast, state-of-the-art techniques, such as Bayesian optimization (BO) and related machine learning (ML) techniques, have recently been applied as an alternative approach in material informatics for high-throughput experimental designs [16–18]. The advances in materials informatics has been primarily focused on utilizing large databases of computational work to accelerate the discovery of new materials [19–22]. The optimization of the properties of a new material often requires extensive parameter studies. Some groups have reported high-throughput experimental work, where ML models were sequentially updated with new measurements [23–25], following a general Bayesian optimization approach. We streamline optimization of LIG patterning conditions within a minimum number of iterations by adopting this iterative, adaptive approach.

Self-adaptive learning systems leverage experience from past applications of machine learning to achieve better results and improve over time [26]. In particular, we investigate the application of techniques for automated parameter tuning through Bayesian model-based optimization [27]. This technique falls under the umbrella of automated parameter tuning, also called hyperparameter configuration, which aims to find the best parameter configuration of an algorithm for a particular application [28]. Techniques for automated parameter tuning usually proceed in an iterative fashion − they predict the configuration to evaluate, and the result of this evaluation informs the predictions for the configuration to evaluate next. At the heart of these techniques are so-called surrogate models, which is cheap to evaluate and allows for a targeted exploration of the parameter space, identifying promising configurations that available resources for evaluations of the underlying process should be directed towards. This family of techniques is often referred to as model-based optimization (MBO), as the optimization process is based on the predictions of the surrogate models that serve as a replacement for the underlying process. Surrogate models are induced using ML, taking an increasing amount of ground-truth data into account between subsequent iterations.

In this study, we describe MBO-assisted laser reduction of graphene on quartz and polyimide. We discovered experimental conditions that lead to LIG patterns with Raman G/D ratios of at least a factor of four higher than those found in the literature. High Raman G/D ratios indicate a high degree of graphene formation in our LIG patterns, which restores the unique properties that are desirable in graphene-based devices. Additionally, we demonstrate the human interpretability of the model that gives insight into the substrate-dependent LIG processing conditions. The mechanisms which govern the formation of LIG patterns are discussed. Since the MBO approach presented here suggests promising configurations iteratively, we consider this work an initial step in the development of human-in-the-loop automated LIG patterning and characterization systems.

2. Experimental setup and methods

2.1. Graphene oxide films

Graphene oxide (GO) was synthesized from graphite using the improved Hummers' method, as it avoids the generation of hazardous gases such as NO and NO_2 from nitrate that is used in the conventional Hummers' method [29]. In this procedure, powdered samples, ground and sieved to 20 μm, were mixed in concentrated H_2SO_4 and H_3PO_4 and placed in an ice bath. Then, $KMnO_4$ was added at a mixture temperature of 35 °C and increased further to 98 °C before termination with ultrapure water (Millipore) and H_2O_2. The filtrate was then washed with HCl and subsequently with water repeatedly until a pH-level of about 6.5 was obtained.

The GO inks were produced using 25 mg of the freeze-dried GO powder, which was diluted in 100 ml deionized water and ultrasonicated with a cooling system. After the sample was centrifuged, the remaining supernatant was repeatedly diluted and ultrasonicated until a 200 ml dilution was obtained. The GO inks were spray-coated onto a 1 cm^2 quartz or polyimide substrate (Kapton HN 125 μm, Dupont) in multiple passes until a thickness of 1 μm was achieved. The GO thickness was verified by scratching the surface and measuring the height using an optical profilometer (VK-X1000, Keyence).

2.2. Laser-induced graphene

Laser-induced graphene (LIG) spots were patterned by reducing GO films deposited on quartz and polyimide, and by carbonization of polyimides directly. We denote GO/Quartz, GO/Polyimide and Polyimide as samples GOQ, GOPI and PI, respectively. The patterning setup is shown in Fig. 1. The deposited GO films were placed in a sample chamber which allows patterning in an air, argon or nitrogen environment with pressures up to 1000 psi. LIG patterns were irradiated using a 532 nm diode-pumped solid-state continuous-wave (CW) laser (Sprout G-12W, Lighthouse Photonics). The laser beam was focused with a 50 × microscope lens to a spot size of 20 μm on the sample surface. Irradiated beam spots were positioned sufficiently far apart from each other to ensure pristine precursor material for each experiment. The sample area is about 1 cm^2, allowing approximately 256, 25, and 25 patterns for samples GOQ, GOPI, and PI, respectively. Taking into account the sample preparation and repeated measurements, we set our experimental budget to the maximum number of successful patterns carried out for our most spatially limited material within a work week, which is 70 runs for PI-based samples. The same number of runs were performed for quartz-based samples for consistency.

The quality of the LIG spots was determined using a Raman spectrometer (Isoplane SCT320, Princeton Instruments). As the sample is irradiated, the laser beam is backscattered and filtered through a long-pass filter to increase the sensitivity of the signal. Using the same laser source for patterning and Raman spectroscopy, the identical spot was characterized *in-situ*. The Raman data for each spot were averaged over 10 measurements with a collection time of 3 s at laser power <10 mW for each measurement. The Raman spectra were post-processed with a linear background
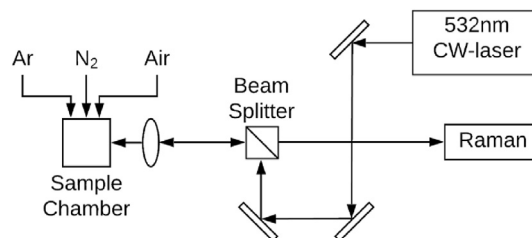

Fig. 1. Schematic of the laser patterning and *in situ* Raman measurement setup.
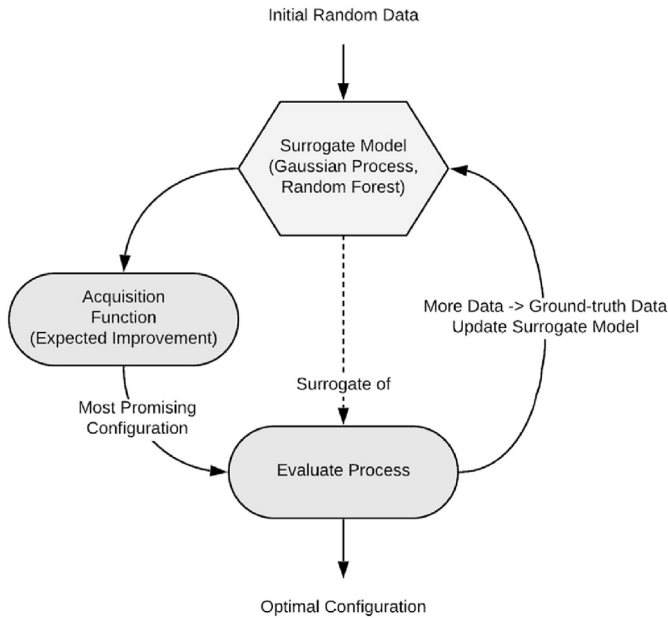
Fig. 2. Schematic of the model-based Bayesian optimization approach used in this study. We use random forests as the surrogate model as the input consists of both continuous numerical and discrete data. The acquisition function is Expected Improvement for maximizing the Raman G/D ratio of LIG.

subtraction to 0 and normalization of the maximum peak to 1. The G- and D-bands were fitted using Lorentzian functions and the ratio of their intensities computed as the ratio of the areas under the fitted functions. The G/D ratios indicate the degree of reduction of GO and is used as a proxy for electric conductivity.

2.3. Model-based optimization

The schematic in Fig. 2 show the procedure of the machine-learning-assisted LIG patterning based on the Bayesian model-based optimization (MBO) algorithm, which is a sequential approach to optimize a black-box function $f(x)$ [30]. In this study, we use the mlrMBO package [31] to model the parameter space, build the surrogate models and determine the most promising configuration for the next evaluation. We do not optimize parameters one-at-a-time [32], but simultaneously to account for possible interactions between them. Here, the G/D ratio $= f(\boldsymbol{x})$ is the objective function specific to our LIG patterns, and x is the process configuration consisting of a complete assignment of values to all parameters, i.e. CW-laser power, irradiation time, gas pressure and type of gas (see Table 1 for limits); for simplicity, we denote 'G/D ratio' as 'ratio' throughout this study unless stated otherwise. The data $\{x_n, \ ratio_n\}_{n=1}^{N}$ obtained from the past N LIG patterns and ratio measurements are used to build a surrogate model to predict the value of $f(\boldsymbol{x})$ at different $\boldsymbol{x}$, substituting the expensive underlying process. As we have a mixture of continuous numerical and discrete categorical parameters, we use a random forest with 500 trees as

our surrogate model. Specifically, the predicted ratio for a point $\boldsymbol{x}$ corresponds to the mean of the predictions across all trees $\mu(\boldsymbol{x})$ and the uncertainty $\sigma(\boldsymbol{x})$ is estimated as the sum of variances over all training points. The point-wise variance is computed as the average of the *jackknife-after-bootstrap* and *infinitesimal jackknife variance* estimates [33], which effectively captures uncertainty due to finite size of the training data.

The objective of the MBO is to maximize the ratio within an experimental budget of 70 runs, which is the largest number of successful patterns performed for our most spatially limited material within a work week. We split the total budget into initial training data of 20 randomly selected configurations to fit the initial surrogate model and 50 iterations of the MBO. The acquisition function proposes the next configuration to evaluate based on the predictions made by the surrogate model. We use the *Expected Improvement (EI)* acquisition function, which searches for the configuration that most likely has a better objective value than the current best measured point [31]. More concretely, the EI takes both the mean $\mu(\boldsymbol{x})$ and uncertainty $\sigma(\boldsymbol{x})$ into account to trade off exploration and exploitation − once the uncertainty becomes sufficiently small for a known good region, the larger uncertainty of unexplored areas of the parameter space will guide it towards that [31].

Our MBO approach applies the focus search algorithm to identify the most promising configurations according to the acquisition function. It shifts from coarser to finer grids for sampling configurations to evaluate the surrogate model on, as even with a cheap surrogate model an exhaustive grid search is prohibitively expensive. The finer grids are centered around the areas where the best configurations were discovered in previous iterations. In this work, the shift is iterated 10 times and the best point over all iterations is chosen. Note that there is no guarantee that this process will find the globally optimal configuration, and no guarantees of convergence. This is because there is no closed functional form for the process we optimize and hence only an exhaustive evaluation of the entire parameter space would allow to identify the global optimum and prove that it is the global optimum. As the evaluations of the process are very expensive (running an experiment), this is infeasible.

To summarize, we begin the iterative parameter tuning process by building an initial surrogate model using random parameter values and selecting the next configuration to evaluate based on the results of the focus search and the acquisition function. Thus, the model proposes new LIG parameters for the next run and the resulting measurement is used to update the surrogate model for the next iteration. This process is iterated until we reach 50 iterations, our stopping criterion. To account for the randomness of the initial data, we performed three experimental runs for each material. The MBO code, dataset and metadata are made available in the supplementary information following the FAIR guiding principles [34].

3. Results

3.1. Maximization of G/D ratio in LIG

Raman spectroscopy is the traditional technique to characterize

Table 1
Parameter space limits for MBO.

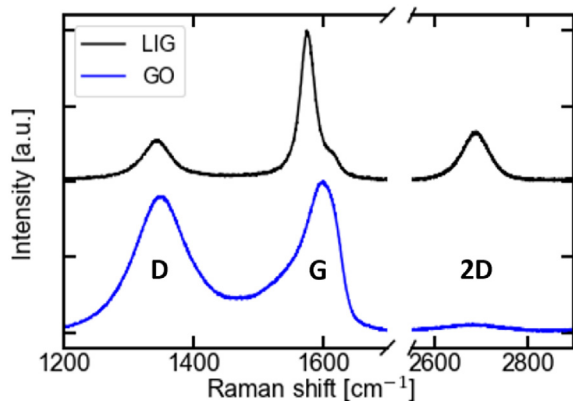| Parameters	Lower limit		Upper limit		Instrument precision	Number of possible values
CW-laser power [W]	0.01		5.55		0.01	554
Irradiation time [s]	0.500		20.000		0.001	195,000
Gas pressure [psi]	0		1000		10	100
Gas type	Argon	Nitrogen	Air		−	3

Fig. 3. Raman spectra of graphene oxide (GO, bottom) and laser-induced graphene (LIG, top). The spectra are offset for clarity. (A colour version of this figure can be viewed online.)

the structural and electronic properties of graphite. It relies on the inelastic scattering of laser photons after they interact with the vibrating molecules in the sample probe. For graphite, Raman experiments extract characteristic information such as the defects (D-band at ~1350 cm^{-1}), in-plane vibrations of sp^2 carbon atoms (G-band at ~1580 cm^{-1}) and the stacking order of the carbon basal planes (2D-band at ~2700 cm^{-1}) [35]. The Raman spectrum of GO and LIG can be distinguished most notably by the presence of the 2D-band in Fig. 3. Although the 2D peak can be fitted with only one Lorentzian peak at ~2700 cm^{-1}, similar to graphene [35], the full-width half-maximum (FWHM) is much larger ~60 cm^{-1} in our LIG, as reported by others [10,36]. In contrast, the 2D-band in bilayer or multilayered graphene is commonly fitted with more than one Lorentzian function [35]. Although the 2D-band was not explicitly optimized in this study, its characteristics are further discussed in Section 3.5. Finally, the G/D ratio indicates the degree of graphitization in the LIG patterns.

A series of three experimental campaigns where conducted for each material. The experimental setup considered parameters and objective were the same, but different batches of GO inks, which were manufactured using the same process, were used to deposit the GO films and different training data points were used. The aim of running a series of experiments was to show that our method to maximize the ratio works with slight variations in the precursor material, as two thin films of graphene oxide are not exactly the same even if they are manufactured using the same process, and to show that we can achieve improvements with different initial training data.

Fig. 4 shows the best-performing optimization runs. For all materials, the random initial parameters for the initial surrogate model are depicted as scatter plots up to the 0th iteration. Note that the performance improves significantly as soon as we explore configurations that were suggested by the model-based parameter optimization approach. Generally, the predictions become more accurate as the distance between the actual and predicted values become smaller with each iteration and as more data are added to the surrogate model. Significant performance improvements are observed in all three campaigns, as evident from the *t*-test results between the randomly sampled and MBO-optimized patterns (Table S1); the corresponding box plots comparing such differences are shown in (Fig. S4).

SEM of the LIG patterns are shown in Fig. 5. Before optimization, the random processing parameters led to LIG patterns with significant damage at the center of the irradiated spot. After optimization, the irradiated pattern is reduced in diameter with no signs

of damage. The porous structures commonly reported in LIG patterns on PI substrates are seen [10]. In contrast, no such structures are observed in GO on quartz substrates, suggesting that they are substrate dependent.

3.2. Interpretations of the surrogate model

Model interpretation is of paramount importance in any ML study. The importance of each parameter can be determined to gain insight into structural features that impact the LIG patterns. We apply partial dependence analysis to obtain post-hoc interpretations of our surrogate models. Similar to descriptor significance analysis, the partial dependence elucidates the effect of a single parameter on a property by marginalizing over all other parameters [37].

For a more robust interpretation of the model, we have trained the surrogate model by combining all the data points from all three campaigns. The partial dependence for the GOPI and PI samples show comparable behavior (Fig. S5). Considering these results, we have combined the data points from six experimental campaigns for both materials into one. The combinations result in a total of 210 and 420 data points for the LIG on substrates quartz (LIGQ) and polyimides (LIGPI), respectively.

3.3. Partial dependence of lasing parameters

The partial dependence plots in Fig. 6a – 6f visualize the marginal relationship between the continuous LIG process parameters and the prediction of the ratio. Note that the ratios in these plots are not measured but predictions made by the surrogate model trained on this data. Therefore, the ratios are not as high as the maximum measured data in the previous section. The grey area denotes how the values vary with all possible values for other parameters i.e. irradiation time, gas pressure and type. For the type of gas, the actual measurements are shown as we cannot compute partial dependencies for categorical parameters.

The partial dependence for laser power shows that the optimal ratio in Fig. 6b is found between 1.9 W–2.5 W. This is in agreement with the threshold power of 2.4 W, at which conversion from PI to LIG occurs [10]. Note that most studies on PI were done with μm-pulsed 10.6 μm lasers, while this study, to the best of our knowledge, is the first LIG investigation using a CW 532 nm laser; in PI, the absorbance at 10.6 μm is twice that of 532 nm [38]. Although we expect some thermal effects from the CW laser, the SEM micrographs in Fig. S5 show that, apart from some striations and cracking of the GO thin film, no significant differences are observed in the morphology between LIG patterned on GOPI and PI. For LIGQ, the optical profilometer micrographs of patterns irradiated at high laser power show depressions in the center of the pattern with no visible melt zones near the edges, which is consistent with a quasi-phase explosion process observed by other groups [39,40]. As the CW laser beam is absorbed, the vaporization of interlayer water builds up internal pressures between the GO sheets until the material is ejected through rapid local heating. The ejecta re-deposit as clusters spattered outwardly in a 380 μm diameter from the irradiation spot (Fig. S6b); these clusters are not visible in lower power regimes (Fig. S6a). Interestingly, clusters were observed for LIGQ but not for LIGPI, which indicates that their origins are substrate-dependent. Additional micro-Raman mapping shows that the clusters in the outer region are not sp^2-hybridized (Fig. S6c), which suggests that the re-deposited material may be re-oxidized, as observed by others [41]. In contrast, high ratios at the edges of the depression center indicate that graphitization occurs following explosive ejection and re-deposition near the irradiated area.

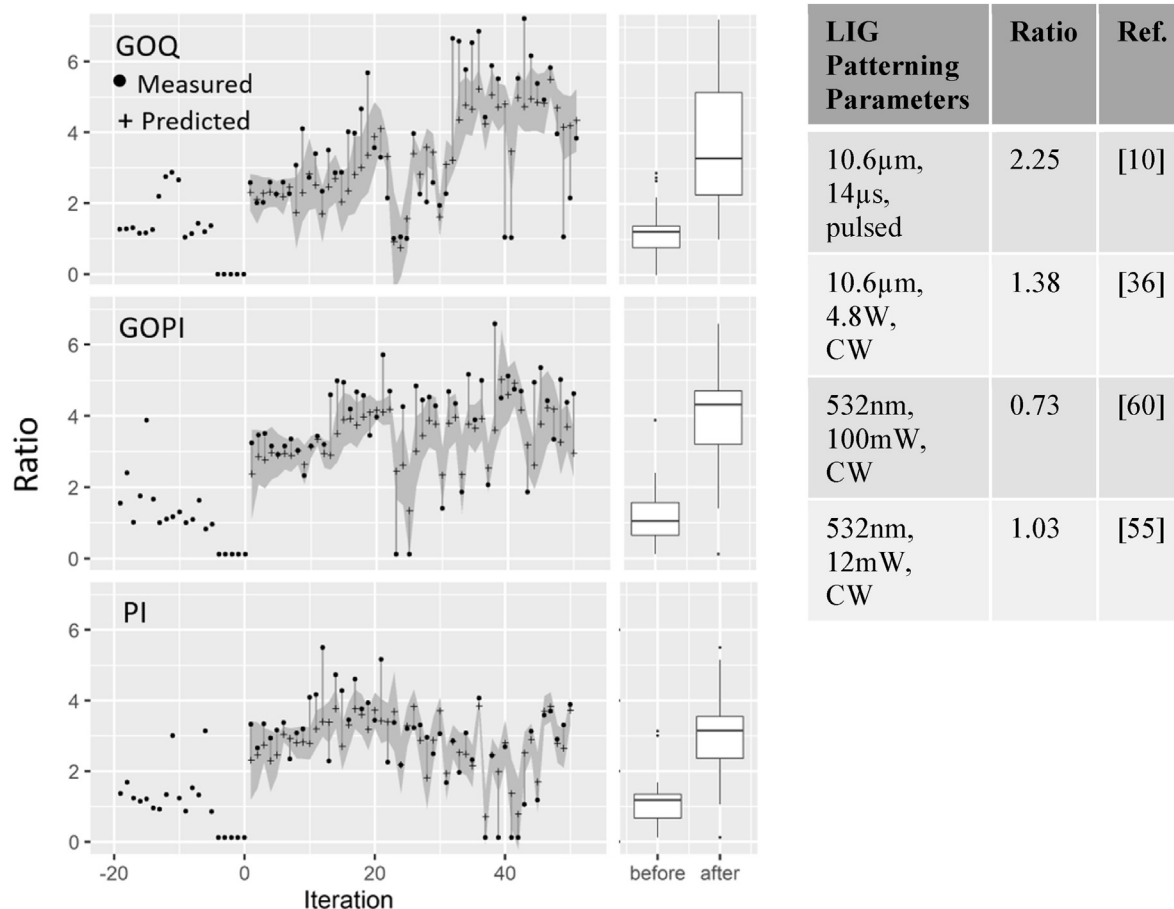The predicted ratios in Fig. 6c and d shows a decreasing trend

LIG Patterning Parameters	Ratio	Ref.
10.6µm, 14µs, pulsed	2.25	[10]
10.6µm, 4.8W, CW	1.38	[36]
532nm, 100mW, CW	0.73	[60]
532nm, 12mW, CW	1.03	[55]

Fig. 4. Progress of G/D ratio optimization for various materials in campaign 1. The box plots show the statistics of the achieved ratios before (iteration <1) and during optimization (iteration≥1); box plots for all campaigns are shown in the supplement (Fig. S4). The results achieved during the optimization are statistically significantly different from the results achieved before for each sample, as evident from t-tests (Table S1). The G/D ratios are improved by a factor of about 3, 4 and 2 in 9, 13 and 1 optimization iterations for GO/quartz (GOQ), GO/polyimide (GOPI) and polyimide (PI), respectively. The grey bounds show the uncertainty of the predictions. State-of-the-art literature values are tabled for comparison.
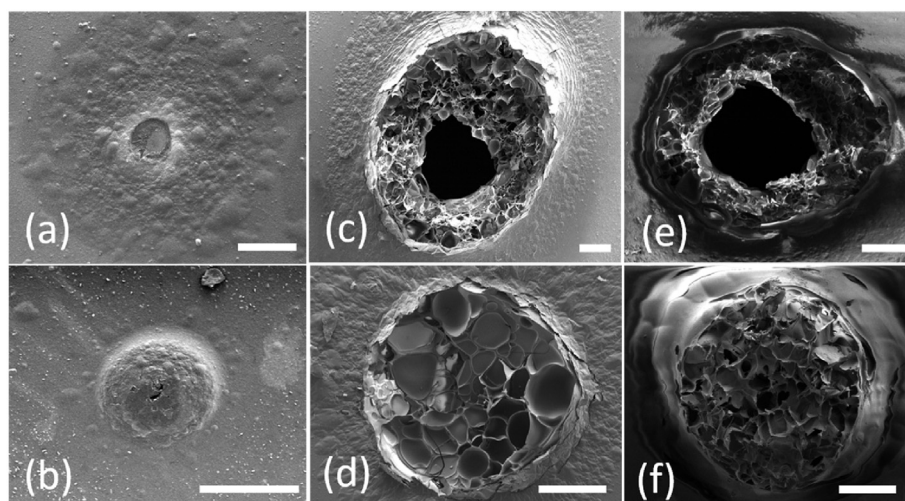

Fig. 5. SEM of the LIG patterned (top) before and (bottom) after optimization for (a),(b) GOQ (c),(d) GOPI and (e),(f) PI. Scale bar is 100 µm.

with irradiation time. In contrast to pulsed laser systems often used in the LIG literature [42], the uninterrupted CW laser results essentially in an infinite "pulse width". The LIG mechanism for CW lasers involves local heat deposition, which deoxygenates the irradiated surface and reorganizes sp^3 to graphene-like sp^2 structures [7]. However, prolonged exposure produced cluster regions
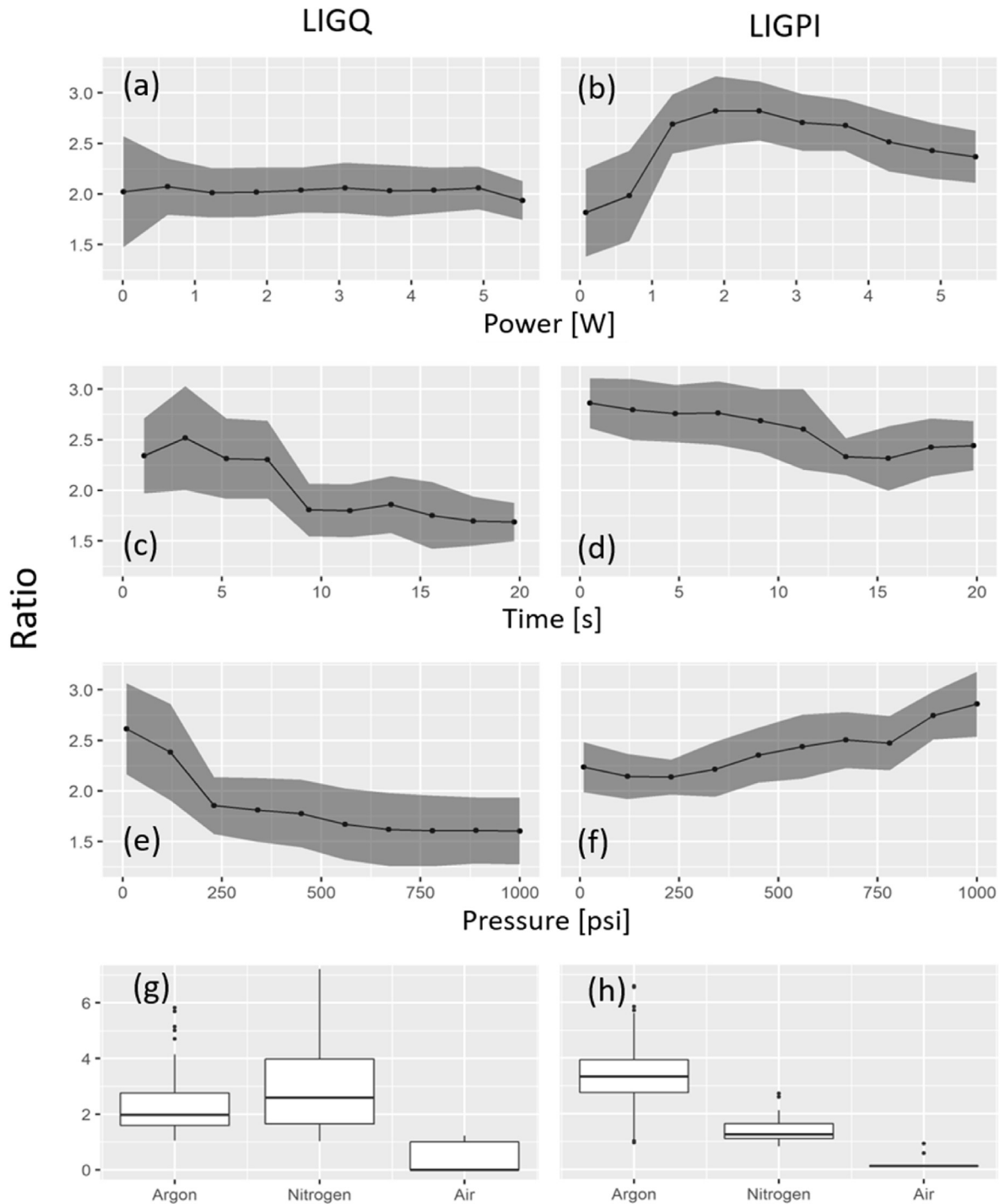
Fig. 6. Partial dependence plots of G/D ratio for different parameters for (a, b) laser power, (c, d) irradiation time, gas (e, f) pressure and (g, h) type of LIG on quartz (LIGQ) and on polyimides (LIGPI), respectively. In both cases, the best ratios are found at lower irradiation times; between powers of 1W−3W for LIGPI; and low and high pressures for LIG on quartz and polyimide substrate, respectively.

that increased in diameter with time (Fig. S7). We believe the extended transfer of energy to the surface induced continuous material ejection and eventually ablates the region within the beam diameter of the laser, causing structural damage that disrupts sp^2 carbon bonds, resulting in a drop of ratios. The surrogate model has learned exactly this effect, as seen in the drop of predicted ratios in Fig. 6c.

Discussions of the partial dependence of laser power and irradiation time on ratios by themselves are rare to find in the literature. This is partly due to the fact that laser power is by itself "time-averaged" and that strong interactions between the two parameters may elucidate LIG mechanisms via instantaneous energy transfer onto the material [43]. Bischl et al. have quantified the post-hoc interpretability of models and show that higher interaction strengths results in less reliable partial dependence analyses [37]. In our ANOVA tests in Tables S2 and S3 we show that the

interactions between power and irradiation time are insignificant, suggesting that our partial dependence analysis is reliable.

3.4. Local environment, plume and thermal effects

A controlled surrounding environment can promote or inhibit chemical reactions, ablation, melting, etc. that are relevant to the LIG patterning process. Here, the LIG approaches in inert gas show the best performance, as seen in Fig. 6g and h. The poor ratios achieved in air may be due to oxidative burning in thick GO [44], resulting in consistent preclusion of this gas type from the configurations proposed by the MBO. In Fig. 6e, the ratio in LIGQ is predicted to increase towards lower pressures, implying that LIG patterning on quartz in vacuum atmosphere helps to reduce defects. This is in agreement with Sokolov et al., who demonstrated successful laser reduction of graphite oxide in vacuum or high purity nitrogen inert gas [41]; our surrogate model has predicted best performance in both environmental conditions.

The role of the inert gas in LIG may be related to a photothermal pathway based on the plume formation, i.e. ablated material being ejected normal to the surface plane that is shaped by pressure gradients [41,45]. In vacuum, the plume expands freely. In inert gas, the expansion is restricted until the pressure within the plume equals the gas pressure. The plume acts as a shield to prevent beam penetration and that generates heat in the material, which, in turn, carbonizes the film. Under these conditions, the low-pressure conditions that are optimal for high ratios in LIGQ suggests large plume expansions of high temperatures. In contrast, the optimum in LIGPI at high pressures confines the plume in a small area at lower temperatures than LIGQ. This is observed clearly by comparing the heat-affected zones, i.e. darkened region outside the delineated circular boundary, as observed in the optical micrographs in Fig. S8, Moreover, the high pressure may reduce the PI substrate from swelling when ablated at increased fluence [45].

The local heating in LIGQ and LIGPI is evident from the Raman shift in Fig. 7. The incident laser is absorbed by the GO or PI surface, causing an increase in local temperature that was observed using *in situ* Raman spectroscopy. The increase in temperature can be estimated by the shift of the G-band according to $T = (\omega - \omega_0)/\chi$, where ω_0 is the frequency of the G-band when temperature T is extrapolated at 0 K, and the temperature coefficient χ is $1.5 \cdot 10^{-2}$ cm^{-1}/K and $2.2 \cdot 10^{-2}$ cm^{-1}/K for graphene [46] and PI [47], respectively. It is justified to use the temperature coefficient of graphene for GO here as the thermal relaxations that govern the laser reduction process is in the ps-scale [48], which is a negligible fraction of the irradiation times used in this study. For LIGQ, the G-band is downshifted by 14 cm^{-1} from the base position of the G-peak ~1585 cm^{-1}, at low pressures (<250 psi), increasing local temperature by ~933 K. For LIGPI, the G-band shift of 15 cm^{-1} at high pressures (>750 psi) increased the local temperature by ~750 K; the position of the G-band varies widely and overlaps in both pressure environments, suggesting higher sensitivity to thermal effects, as expected from soft substrates such as PI. The differences in temperature increase show that the underlying substrate plays an important role as a heat sink in graphene formation, as observed by others [44]. As the thermal diffusivity of quartz is a factor of seven larger than PI [49], we believe that the net photothermal effect from the plume and the heat sink promotes LIG patterns to form.

3.5. 2D-band characteristics of LIG

For a rigorous identification of graphene or LIG, the analysis of the G/D ratio alone may be insufficient as this parameter may be affected by the amorphization trajectory described by Ferrari and Robertson [50]. Hence, the characteristics of the 2D-band, particularly with respect to the G/D ratio that has been optimized in this study, will be further discussed.

The analysis of the 2D/G parameter presented in Fig. 8 shows that, apart from some outliers, the 2D-band is mostly present for both LIGQ and LIGPI with a larger 2D/G distribution for the latter, presumably due to the substrate-dependent thermal effects discussed in the previous section. The 2D-band is an overtone of the D-band, but unlike the latter, it is not activated near defects. As a result, the 2D-band can be present in LIG even in the absence of the D-band.

The 2D-band can be analyzed to determine graphene layer thickness. For monolayer graphene, the 2D-band is observed to be one symmetrical peak with a FWHM of ~30 cm^{-1} [51]. With the addition of successive layers, others report broadening and splitting of the 2D-band such that the distinct band shape can differentiate between single and multilayer graphene for layer thickness of less than 4 layers [51]. Although the FWHM reported here generally decreases with increasing G/D ratio, the 2D-bands in our samples are typically twice as broad as those reported for monolayer graphene, as seen in other LIG reports [10,36]; they have a symmetrical profile (Fig. 8d) more closely related to 2D graphite with its layers randomly stacked along the c-axis [52].

It is worth pointing out that monolayer graphene can be identified by analyzing the ratio between the 2D- and the G-band. The 2D/G ratios in Fig. 8a and b generally increase with G/D ratio up to
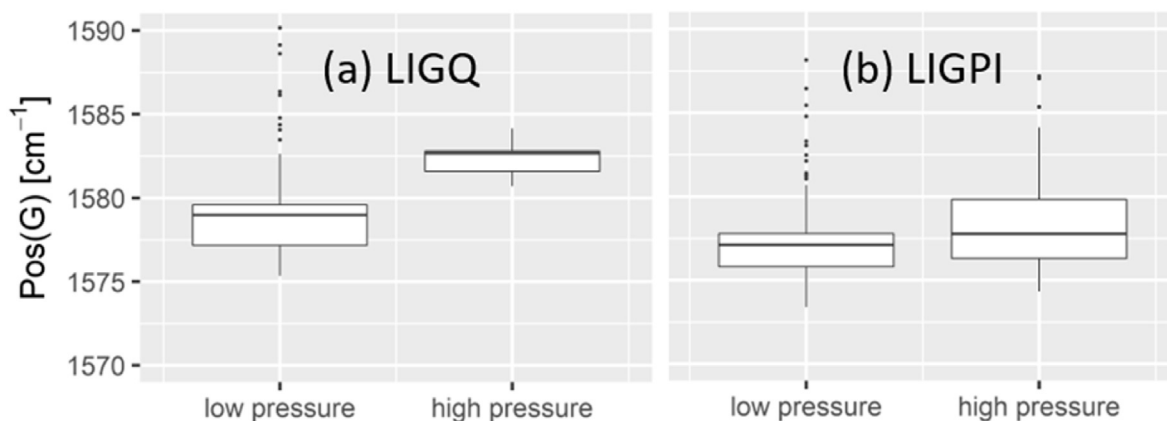

Fig. 7. Position of the G-band at low (<250 psi) and high (>750psi) pressures for (a) LIGQ and (b) LIGPI samples. In contrast to LIGPI, the Raman shift in LIGQ at high gas pressures indicate a larger local temperature increase. The quality of LIG depends on the net thermal effect and the underlying substrate. At high pressures for LIGPI, the localized heating is restricted, promoting carbonization. On quartz, high-quality LIG is patterned at low gas pressure that expands local heating.
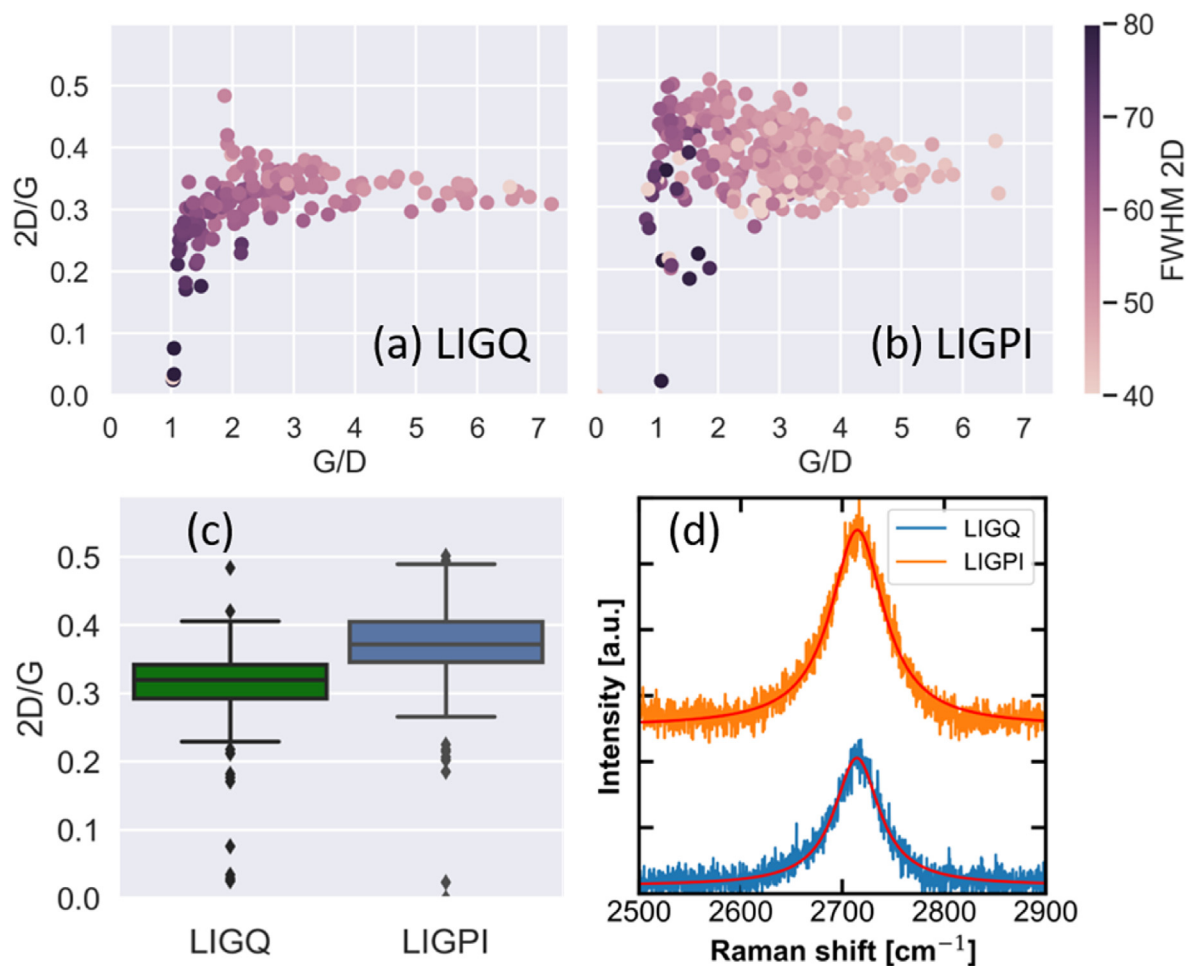
Fig. 8. The 2D/G ratio for (a) LIGQ and (b) LIGPI as a function of G/D ratio, which was optimized using MBO. The color bar shows the FWHM(2D) in cm^{-1}; FWHM(2D) and G/D ratios are negatively correlated (Spearman coefficients: (a) −0.79 and (b) −0.64). (c) Boxplot for the 2D/G ratio distributions and (d) symmetrical 2D-band profile for both LIG substrates. (A colour version of this figure can be viewed online.)

G/D ~2 and plateau at medians of 0.32 and 0.38, respectively. The maximum 2D/G values presented for LIG here are comparable to those reported in the literature (see Table 2). Note, in comparison to the G/D parameter, the 2D/G parameter for LIG is not widely reported and the values presented here are roughly estimated. These values range between a quarter to half of the values typically observed in defect-free single layer graphene materials (2D/G ~ 2) [53]. Interestingly, to the best of our knowledge, the D-band does not diminish through the laser induction process and thus high-quality LIG are not defect-free. Therefore, it is reasonable to take the D-band into account during single-objective optimization of G/D ratios. Nevertheless, through additional analysis of the 2D/G ratio, FWHM(2D) and the 2D-band profile we have deduced high-quality LIG.

3.6. Related work

The best ratios averaged over the three LIG campaigns are 5.36, 7.13 and 5.38 for GOQ, GOPI and PI, respectively, and were achieved within 50 optimization iterations. To note, while this has cost a week of experimentation, prior study without MBO-assistance required not only over a month's work but also yielded suboptimal results [54]. While the base ratio was measured to be about 1 for unreduced GO films, the characteristic Raman G-, D- and 2D-features were not found in non-irradiated polyimides. A list of LIG

parameter conditions in the literature with the corresponding ratios are shown in Table 2. To the best of our knowledge, other groups with comparable experimental setups, i.e. 532 nm CW laser patterning of GO thin films, demonstrate a maximum ratio of 1.03 [55]. Hawes et al. have carbonized PI substrates using CW CO_2 laser and demonstrated a ratio of 1.38 [11]. While we acknowledge that a higher ratio of 2.25 has been observed in LIG on PI [10], it is not trivial to have a direct comparison of our work with that in the community as the results of laser-material interactions are highly dependent on the characteristics of the laser system e.g. pulse width and wavelength. We therefore prioritize and compare studies using CW lasers, since the underlying mechanism for CW laser reduction is thermally mediated [7]. The introduction of automated parameter tuning with surrogate models improves performance in a small number of iterations with relatively little experimental effort by a factor of at least four. We emphasize that the advantage of automated parameter tuning used here is not limited specifically to our experimental setup but can be applied in other contexts as well, e.g. pulsed laser systems.

3.7. Discussion

There are several avenues for future studies. First, despite our reliable model interpretations, we believe that our understanding of the underlying LIG processes has not necessarily improved. With

Table 2
List of laser-induced graphene (LIG) parameter conditions from various precursor materials and their Raman G/D and 2D/G ratios.

Laser Type	Patterning Parameters	Precursor Material/Substrate	G/D Ratio	2D/G Ratio	Ref
Pulsed	790 nm, 120fs	GO/glass	1.10	0.13	[56]
Pulsed	10.6 μm, 2.4W	Hydrated graphite oxide film	1.28	–	[57]
Pulsed	355 nm, 20ns	Graphite oxide film	1.15	0.05	[58]
Pulsed	522 nm, 500fs	PI	0.86	0.06	[11]
Pulsed	10.6 μm, 14 μs	PI	2.25	0.95	[10]
Pulsed	10.6 μm, 14 μs	PI	1.03	0.46	[59]
CW	10.6 μm, 4.8W	PI	1.38	0.48	[36]
CW	532 nm, 100 mW	Thin film GO/glass	0.73	–	[60]
CW	663 nm, 80 mW	GO/Quartz	0.93	–	[61]
CW	788 nm, 5 mW	Graphite oxide/polycarbonate	0.94	0.26	[62]
CW	532 nm, 12 mW	Thin film GO/SiO$_2$/Si	1.03	0.13	[55]
CW	532 nm, <5.5W, <1000 psi	Thin film GO/quartz	5.36	0.49	Our MBO approach
		GO/PI	7.13	0.52	
		PI	5.38	0.51	

a view to develop explainable artificial intelligence systems, leveraging these models would allow us to close the scientific loop and have AI work in tandem with human researchers to not only achieve better experimental results, but also to develop new theories. More explicitly, the MBO partial dependence analysis has guided us to find the physical domains to investigate further post-optimization, and from that we formulated a substrate-dependent mechanism in LIG formation based on thermal and plume effects in a local environment. Future work could include ML approaches that considers the discrepancies between simulation and experiments, which is expected to outperform random ML training approaches. The analysis of the partial dependencies we performed in this paper is a valuable first step to integrate physics within ML.

Second, while we have achieved good ratios, the simultaneous optimization of other objectives, such as the electric and thermal properties, can be beneficial to fabricate electronic devices. A common problem in multi-objective optimizations is that one property of the material cannot be improved without degrading another. Instead, an optimal boundary, the so-called Pareto front, defines the trade-off between configurations that are optimal with respect to at least one property. Multi-objective optimization has been demonstrated to be data exhaustive [63,64]. Most materials discovery studies therefore focus on single-objective optimization, which can support multi-objective optimization by combining all objectives into one. Another practical challenge is that often measurements can only be taken at multiple levels. For example, Raman characterization of a material can happen immediately after a LIG patterning has been performed, but measurements of electric conductivity using a four-point probe can only be performed after an experimental campaign is finished as this requires removal of the sample from the reaction chamber. The integration of such multi-level measurements that occur at different frequencies into a Bayesian optimization process would potentially allow further improvements.

4. Conclusion

We have demonstrated the application of state-of-the-art automated parameter optimization techniques to laser-induced graphene (LIG) patterning and improved the quality of LIG patterns based on Raman G/D ratios reported in the literature by at least a factor of four. The best LIG ratios were achieved within 50 configurations suggested by the MBO. The initial surrogate models were trained with random parameter evaluations that are independent of the skills and experience of individual researchers – our method does not rely on skilled operators to "guide" it towards good results. Further, our system does also not require a background in machine learning, and the achieved improvements are demonstrated to be reliable and reproducible. We further demonstrate how the surrogate model can be used to improve our understanding of the underlying processes for LIG patterned on quartz and on polyimide. The partial dependence analysis shows that the LIG mechanism is governed by substrate-dependent local thermal effects and plume formations. This conclusion is supported by optical characterizations.

CRediT authorship contribution statement

Hud Wahab: Writing - original draft, Data curation, Formal analysis, Supervision. **Vivek Jain:** Writing - original draft, Data curation, Formal analysis. **Alexander Scott Tyrrell:** Writing - original draft, Data curation, Formal analysis. **Michael Alan Seas:** Writing - original draft, Data curation, Formal analysis, Conceptualization. **Lars Kotthoff:** Writing - original draft, Data curation, Formal analysis. **Patrick Alfred Johnson:** Writing - original draft, Conceptualization, Supervision.

Declaration of competing interest

The authors declare that they have no known competing financial interests or personal relationships that could have appeared to influence the work reported in this paper.

Acknowledgements

the University of Wyoming's Engineering Initiative of the College of Engineering and Applied Science and School of Energy Resources.

Appendix A. Supplementary data

Supplementary data related to this article can be found at https://doi.org/10.1016/j.carbon.2020.05.087.

References

[1] T. Stensitzki, Y. Yang, V. Kozich, A.A. Ahmed, F. Kössl, O. Kühn, et al., Acceleration of a ground-state reaction by selective femtosecond-infrared-laser-pulse excitation, Nat. Chem. 10 (2) (2018) 126–131.
[2] A. Vyatskikh, S. Delalande, A. Kudo, X. Zhang, C.M. Portela, J.R. Greer, Additive manufacturing of 3D nano-architected metals, Nat. Commun. 9 (1) (2018) 593.
[3] H. Wahab, J. Gröninger, K. Dickmann, P. Bruns, M. Voß, I. Kardosh, et al., Optimization of laser cutting quality with design of experiments, Laser Technik J. 11 (5) (2014) 27–31.
[4] J.B. Park, W. Xiong, Y. Gao, M. Qian, Z.Q. Xie, M. Mitchell, et al., Fast growth of graphene patterns by laser direct writing, Appl. Phys. Lett. 98 (123109) (2011) 1–3.
[5] D. Wei, J.I. Mitchell, C. Tansarawiput, W. Nam, M. Qi, P.D. Ye, et al., Laser direct synthesis of graphene on quartz, Carbon 53 (2013) 374–379.
[6] A.C. Ferrari, F. Bonaccorso, V. Fal'ko, K.S. Novoselov, S. Roche, P. Boggild, et al., Science and technology roadmap for graphene, related two-dimensional crystals, and hybrid systems, Nanoscale 7 (11) (2015) 4598–4810.
[7] R. Arul, R.N. Oosterbeek, J. Robertson, G. Xu, J. Jin, M.C. Simpson, The mechanism of direct laser writing of graphene features into graphene oxide films involves photoreduction and thermally assisted structural rearrangement, Carbon 99 (2016) 423–431.
[8] D.A. Dikin, S. Stankovich, E.J. Zimney, R.D. Piner, G.H.B. Dommett, G. Evmenenko, et al., Preparation and characterization of graphene oxide paper, Nature 448 (7152) (2007) 457–460.
[9] S.H. Lee, H.B. Lee, Y. Kim, J.R. Jeong, M.H. Lee, K. Kang, Neurite guidance on laser-scribed reduced graphene oxide, Nano Lett. 18 (12) (2018) 7421–7427.
[10] J. Lin, Z. Peng, Y. Liu, F. Ruiz-Zepeda, R. Ye, E.L.G. Samuel, et al., Laser-induced porous graphene films from commercial polymers, Nat. Commun. 5 (5714) (2014) 1–8.
[11] J.B. In, B. Hsia, J.-H. Yoo, S. Hyun, C. Carraro, R. Maboudian, et al., Facile fabrication of flexible all solid-state micro-supercapacitor by direct laser writing of porous carbon in polyimide, Carbon 83 (2015) 144–151.
[12] Z. Peng, J. Lin, R. Ye, E.L.G. Samuel, J.M. Tour, Flexible and stackable laser-induced graphene supercapacitors, ACS Appl. Mater. Interfaces 7 (5) (2015) 3414–3419.
[13] R. Ye, Z. Peng, T. Wang, Y. Xu, J. Zhang, Y. Li, et al., In situ formation of metal oxide nanocrystals embedded in laser-induced graphene, ACS Nano 9 (9) (2015) 9244–9251.
[14] R.A. Fisher, The Design of Experiments, Oliver & Boyd, Oxford, England, 1935.
[15] R.K. Roy, A Primer on the Taguchi Method, Society of Manufacturing Engineers, 1990.
[16] P. Nikolaev, D. Hooper, F. Webber, R. Rao, K. Decker, M. Krein, et al., Autonomy in materials research: a case study in carbon nanotube growth, Npj Comput. Mater. 2 (16031) (2016) 1–6.
[17] K. Alberi, M.B. Nardelli, A. Zakutayev, L. Mitas, S. Curtarolo, A. Jain, et al., The 2019 materials by design roadmap, J. Phys. Appl. Phys. 52 (1) (2018) 1–48, 013001.
[18] S.P. Ong, Accelerating materials science with high-throughput computations and machine learning, Comput. Mater. Sci. 161 (2019) 143–150.
[19] K. Choudhary, I. Kalish, R. Beams, F. Tavazza, High-throughput identification and characterization of two-dimensional materials using density functional theory, Sci. Rep. 7 (1) (2017) 1–16, 5179.
[20] P.V. Balachandran, A.A. Emery, J.E. Gubernatis, T. Lookman, C. Wolverton, A. Zunger, Predictions of new ABO3 perovskite compounds by combining machine learning and density functional theory, Phys. Rev. Mater. 2 (4) (2018) 1–18, 043802.
[21] V. Stanev, C. Oses, A.G. Kusne, E. Rodriguez, J. Paglione, S. Curtarolo, et al., Machine learning modeling of superconducting critical temperature, Npj Comput. Mater. 4 (1) (2018) 1–14, 29.
[22] O. Isayev, C. Oses, C. Toher, E. Gossett, S. Curtarolo, A. Tropsha, Universal fragment descriptors for predicting properties of inorganic crystals, Nat. Commun. 8 (1) (2017) 1–12, 15679.
[23] Z. Hou, Y. Takagiwa, Y. Shinohara, Y. Xu, K. Tsuda, Machine-learning-assisted development and theoretical consideration for the Al2Fe3Si3 thermoelectric material, ACS Appl. Mater. Interfaces 11 (12) (2019) 11545–11554.
[24] F. Ren, L. Ward, T. Williams, K.J. Laws, C. Wolverton, J. Hattrick-Simpers, et al., Accelerated discovery of metallic glasses through iteration of machine learning and high-throughput experiments, Sci. Adv. 4 (4) (2018) 1–11, eaaq1566.
[25] Y.K. Wakabayashi, T. Otsuka, Y. Taniyasu, H. Yamamoto, H. Sawada, Improved adaptive sampling method utilizing Gaussian process regression for prediction of spectral peak structures, APEX 11 (11) (2018) 1–4, 112401.
[26] R. Vilalta, Y. Drissi, A perspective view and survey of meta-learning, Artif. Intell. Rev. 18 (2) (2002) 77–95.
[27] J. Vanschoren, Meta-Learning, vol. 1810, A Survey, 2018, pp. 1–29, 03548.
[28] H.H. Hoos, Automated algorithm configuration and parameter tuning, in: Y. Hamadi, E. Monfroy, F. Saubion (Eds.), Autonomous Search, Springer Berlin Heidelberg, Berlin, Heidelberg, 2012, pp. 37–71.
[29] D.C. Marcano, D.V. Kosynkin, J.M. Berlin, A. Sinitskii, Z. Sun, A. Slesarev, et al., Improved synthesis of graphene oxide, ACS Nano 4 (8) (2010) 4806–4814.
[30] D.R. Jones, M. Schonlau, W.J. Welch, Efficient global optimization of expensive black-box functions, J. Global Optim. 13 (4) (1998) 455–492.
[31] B. Bischl, J. Richter, J. Bossek, D. Horn, J. Thomas, M. Lang, mlrMBO, A Modular Framework for Model-Based Optimization of Expensive Black-Box Functions, 2018, pp. 1–26, 1703.03373.
[32] Y.K. Wakabayashi, T. Otsuka, Y. Krockenberger, H. Sawada, Y. Taniyasu, H. Yamamoto, Machine-learning-assisted thin-film growth: Bayesian optimization in molecular beam epitaxy of SrRuO3 thin films, Apl. Mater. 7 (10) (2019) 1–8, 101114.
[33] S. Wager, T. Hastie, B. Efron, Confidence intervals for random forests: the jackknife and the infinitesimal jackknife, J. Mach. Learn. Res. 15 (1) (2014) 1625–1651.
[34] M.D. Wilkinson, M. Dumontier, I.J. Aalbersberg, G. Appleton, M. Axton, A. Baak, et al., The FAIR Guiding Principles for scientific data management and stewardship, Sci. Data 3 (1) (2016) 1–9, 160018.
[35] A.C. Ferrari, J.C. Meyer, V. Scardaci, C. Casiraghi, M. Lazzeri, F. Mauri, et al., Raman spectrum of graphene and graphene layers, Phys. Rev. Lett. 97 (18) (2006) 187401.
[36] G.F. Hawes, D. Yilman, B.S. Noremberg, M.A. Pope, Supercapacitors fabricated via laser-induced carbonization of biomass-derived poly(furfuryl alcohol)/graphene oxide composites, ACS Appl. Nano Mater. 2 (10) (2019) 6312–6324.
[37] C. Molnar, G. Casalicchio, B. Bischl, Quantifying Model Complexity via Functional Decomposition for Better Post-Hoc Interpretability, 2019, pp. 1–12, 1904.03867.
[38] J. Hillman, Y. Sukhman, D. Miller, M. Oropeza, C. Risser, Multiwave hybrid laser processing of micrometer scale features for flexible electronic applications, SPIE Proc. 9736 (2016) 1–8.
[39] Z. Chen, A. Vertes, Early plume expansion in atmospheric pressure mid-infrared laser ablation of water-rich targets, Phys. Rev. 77 (3) (2008) 1–9, 036316.
[40] D.A. Sokolov, K.R. Shepperd, T.M. Orlando, formation of graphene features from direct laser-induced reduction of graphite oxide, J. Phys. Chem. Lett. 1 (18) (2010) 2633–2636.
[41] D.A. Sokolov, C.M. Rouleau, D.B. Geohegan, T.M. Orlando, Excimer laser reduction and patterning of graphite oxide, Carbon 53 (2013) 81–89.
[42] R. Ye, D.K. James, J.M. Tour, Laser-induced graphene: from discovery to translation, Adv. Mater. 31 (1) (2019) 1–15, 1803621.
[43] J.J. Gaumet, A. Wakisaka, Y. Shimizu, Y. Tamori, Energetics for carbon clusters produced directly by laser vaporization of graphite: dependence on laser power and wavelength, J. Chem. Soc., Faraday Trans. 89 (11) (1993) 1667–1670.
[44] G.H. Han, S.J. Chae, E.S. Kim, F. Güneş, I.H. Lee, S.W. Lee, et al., Laser thinning for monolayer graphene formation: heat sink and interference effect, ACS Nano 5 (1) (2011) 263–268.
[45] E.R. Mamleyev, S. Heissler, A. Nefedov, P.G. Weidler, N. Nordin, V.V. Kudryashov, et al., Laser-induced hierarchical carbon patterns on polyimide substrates for flexible urea sensors, Npj Flex. Electron. 3 (1) (2019) 1–11.
[46] I. Calizo, A.A. Balandin, W. Bao, F. Miao, C.N. Lau, Temperature dependence of the Raman spectra of graphene and graphene multilayers, Nano Lett. 7 (9) (2007) 2645–2649.
[47] S. Venkatachalam, M. Depriester, A.H. Sahraoui, B. Capoen, M.R. Ammar, D. Hourlier, Thermal conductivity of Kapton-derived carbon, Carbon 114 (2017) 134–140.
[48] X. Zhao, Z.-B. Liu, W.-B. Yan, Y. Wu, X.-L. Zhang, Y. Chen, et al., Ultrafast carrier dynamics and saturable absorption of solution-processable few-layered graphene oxide, Appl. Phys. Lett. 98 (12) (2011) 1–4, 121905.
[49] E.R.G. Eckert, E.R.G. Eckert, R.M. Drake, Heat and Mass Transfer, McGraw-Hill, 1959.
[50] A.C. Ferrari, J. Robertson, Interpretation of Raman spectra of disordered and amorphous carbon, Phys. Rev. B 61 (20) (2000) 14095–14107.
[51] A.C. Ferrari, D.M. Basko, Raman spectroscopy as a versatile tool for studying the properties of graphene, Nat. Nanotechnol. 8 (2013) 235.
[52] M.A. Pimenta, G. Dresselhaus, M.S. Dresselhaus, L.G. Cançado, A. Jorio, R. Saito, Studying disorder in graphite-based systems by Raman spectroscopy, Phys. Chem. Chem. Phys. 9 (11) (2007) 1276–1290.
[53] Z. Sun, Z. Yan, J. Yao, E. Beitler, Y. Zhu, J.M. Tour, Growth of graphene from solid carbon sources, Nature 468 (7323) (2010) 549–552.
[54] M.A. Seas, Ultrahigh Temperature Annealing and Laser Irradiation: a Potential Route to Producing Valuable Electronic Materials from Coal, Masters' Thesis, Chemical Engineering, University of Wyoming, 2018, p. 70. Accessed: 2020/03/04, http://search.proquest.com/docview/2115849737?accountid=14793.
[55] Y. Tao, B. Varghese, M. Jaiswal, S. Wang, Z. Zhang, B. Oezyilmaz, et al., Localized insulator-conductor transformation of graphene oxide thin films via focused laser beam irradiation, Appl. Phys. A 106 (3) (2012) 523–531.
[56] Y. Zhang, L. Guo, S. Wei, Y. He, H. Xia, Q. Chen, et al., Direct imprinting of microcircuits on graphene oxides film by femtosecond laser reduction, Nano Today 5 (1) (2010) 15–20.

[57] W. Gao, N. Singh, L. Song, Z. Liu, A.L.M. Reddy, L. Ci, et al., Direct laser writing of micro-supercapacitors on hydrated graphite oxide films, Nat. Nanotechnol. 6 (496) (2011) 1–5.

[58] R. Kumar, R. Savu, E. Joanni, A.R. Vaz, M.A. Canesqui, R.K. Singh, et al., Fabrication of interdigitated micro-supercapacitor devices by direct laser writing onto ultra-thin, flexible and free-standing graphite oxide films, RSC Adv. 6 (88) (2016) 84769–84776.

[59] D.X. Luong, A.K. Subramanian, G.A.L. Silva, J. Yoon, S. Cofer, K. Yang, et al., Laminated object manufacturing of 3D-printed laser-induced graphene foams, Adv. Mater. 30 (28) (2018) 1–6, 1707416.

[60] E. Orabona, A. Ambrosio, A. Longo, G. Carotenuto, L. Nicolais, P. Maddalena, Holographic patterning of graphene-oxide films by light-driven reduction, Opt. Lett. 39 (14) (2014) 4263–4266.

[61] Y. Zhou, Q. Bao, B. Varghese, L.A.L. Tang, C.K. Tan, C.-H. Sow, et al., Microstructuring of graphene oxide nanosheets using direct laser writing, Adv. Mater. 22 (1) (2010) 67–71.

[62] V. Strong, S. Dubin, M.F. El-Kady, A. Lech, Y. Wang, B.H. Weiller, et al., Patterning and electronic tuning of laser scribed graphene for flexible all-carbon devices, ACS Nano 6 (2) (2012) 1395–1403.

[63] F.A.C. Viana, T.W. Simpson, V. Balabanov, V. Toropov, Special section on multidisciplinary design optimization: metamodeling in multidisciplinary design optimization: how far have we really come? AIAA J. 52 (4) (2014) 670–690.

[64] K. Deb, Multi-objective optimisation using evolutionary algorithms: an introduction, in: L. Wang, A.H.C. Ng, K. Deb (Eds.), Multi-objective Evolutionary Optimisation for Product Design and Manufacturing, Springer London, London, 2011, pp. 3–34.